Research Article Vol. 30, No. 4 / 14 Feb 2022 / Optics Express 5709
Optics EXPRESS

Propagation of Bessel-correlated specular and antispecular beams

DIPANJAN DAS,[1] ATRI HALDER,[1,*] HENRI PARTANEN,[1,2] MATIAS KOIVUROVA,[3] AND JARI TURUNEN[1]

[1] University of Eastern Finland, P.O. Box 111, FI-80101 Joensuu, Finland
[2] Current address: Dispelix Oy, Metsänneidonkuja 10, FI-02130 Espoo, Finland
[3] Faculty of Engineering and Natural Sciences, Photonics, Tampere University, FI-33720 Tampere, Finland
[*] tri.halder@uef.fi

Abstract: We address the specular properties of Bessel-correlated fields, generated by illuminating a tilted rotating plane-parallel glass plate with a coherent Gaussian beam and passing the output beam though a mirror-based wavefront folding interferometer. This device allows us to produce beams whose specular properties are preserved in propagation. In the far zone, the specular nature of these partially coherent fields is shown to produce intensity-profile oscillations in the sub-diffraction-limit scale. The analytical results at various propagation distances are verified experimentally by using another wavefront-folding interferometer for coherence measurements.

© 2022 Optica Publishing Group under the terms of the Optica Open Access Publishing Agreement

1. Introduction

The concept of specular cross-spectral density (CSD) functions was introduced by Gori and his collaborators [1] already in 1987. However, the properties and propagation features of specular beams have received only little attention since then [2,3], and the first experimental demonstrations were provided only recently [4]. In Ref. [4], beamlike fields with specular (and antispecular) CSDs were synthesized from Gaussian Schell-model incident beams using a traditional retroreflecting prism-based wavefront-folding interferometer (WFI) and characterized using Young's interferometer.

In the experiments reported in Ref. [4], the characteristic features of specular and antispecular fields (such as the cross-like structure of the CSD) were verified, but only at the plane of the beam waist. Studies of propagated beams proved virtually impossible because diffraction from the prism edges of the interferometer produces a pronounced cross-like and rapidly expanding disturbance in the intensity profile of the field. This phenomenon effectively hides the specular characteristics of the field, however sharp the prism edges are. However, recent developments in coherence-measurement devices have lead to the introduction of WFI variants based on planar mirrors instead of prisms [5,6]. These devices are free from prism-edge diffraction effects and thereby excellent candidates also for performing the specular transformation to create disturbance-free specular or antispecular beams. In this paper we use such a device to create Bessel-correlated beams with specular CSDs, and to study their free-space propagation.

We begin with an introduction of the 2D specular transformation in Sec. 2, which is realizable with a 2D WFI, and to describe the free-space propagation of specular fields in general. In Sec. 3 we proceed to define the specific class of Bessel-correlated fields that we employ for our experiments and consider their propagation features after the specular (or antispecular) transformation. Their main physical features are highlighted in Sec. 4, and illustrated in Sec. 5. In Sec. 6 we describe the experimental setup and provide verification of the main theoretical results, including the super-oscillating nature of the far-zone intensity distribution of partially coherent specular beams. Finally, conclusions are drawn and some possible future directions of the work are discussed in Sec. 7.

#452308 https://doi.org/10.1364/OE.452308
Journal © 2022 Received 26 Dec 2021; revised 19 Jan 2022; accepted 19 Jan 2022; published 7 Feb 2022

Optics EXPRESS

2. Specular transformation

Let us consider a spatially partially coherent light beam propagating along the z-axis, assuming that the CSD at a plane $z = z_0$ has the form

$$W_0(x_1, y_1, x_2, y_2, z_0) = \langle E_0^*(x_1, y_1, z_0) E_0(x_2, y_2, z_0) \rangle, \tag{1}$$

where $E_0(x, y, z)$ is the electric field at the position (x, y, z) in cartesian coordinates, and we have left the dependence of the CSD on the angular frequency ω implicit for brevity. Specular and antispecular fields can be generated from any arbitrary field via the specular transformation

$$\begin{aligned} W(x_1, y_1, x_2, y_2, z_0) = &\frac{1}{2}\left[W_0(x_1, -y_1, x_2, -y_2, z_0) + W_0(-x_1, y_1, -x_2, y_2, z_0)\right] \\ &+ \frac{1}{2}\left[W_0(x_1, -y_1, -x_2, y_2, z_0)\exp(i\phi) + W_0(-x_1, y_1, x_2, -y_2, z_0)\exp(-i\phi)\right], \end{aligned} \tag{2}$$

where ϕ is a real number that can be interpreted as a phase delay. The transformed field is called specular if $\phi = 2\pi n$ and antispecular if $\phi = 2\pi n + \pi/2$, with n being an integer. Therefore, for these two phase-delay values, the CSD has the property

$$W(-x_1, -y_1, x_2, y_2, z_0) = \pm W(x_1, y_1, x_2, y_2, z_0), \tag{3}$$

which corresponds to a specular (antispecular) CSD if the positive (negative) sign is chosen on the right-hand side of the expression. One can also define fields that are specular or antispecular in one dimension by demanding either that $W(-x_1, y_1, x_2, y_2, z_0) = \pm W(x_1, y_1, x_2, y_2, z_0)$ or that $W(x_1, -y_1, x_2, y_2, z_0) = \pm W(x_1, y_1, x_2, y_2, z_0)$. Transformations of the type indicated in Eq. (2) can be performed by first splitting the input field into two parts and then recombining them after introducing a path-length difference corresponding to the desired phase difference ϕ.

The k-space (far zone) behaviour of the field is specified by the angular correlation function (ACF), which describes coherence between different spatial frequencies (k_x, k_y). The ACF is defined as

$$\begin{aligned} T(k_{x1}, k_{y1}, k_{x2}, k_{y2}) = &\frac{1}{(2\pi)^4} \iiiint_{-\infty}^{\infty} W(x_1, y_1, x_2, y_2, z_0) \\ &\times \exp\left[i\left(k_{x1}x_1 + k_{y1}y_1 - k_{x2}x_2 - k_{y2}y_2\right)\right] \mathrm{d}x_1 \mathrm{d}y_1 \mathrm{d}x_2 \mathrm{d}y_2. \end{aligned} \tag{4}$$

In analogy with Eq. (3), the field is called specular or antispecular in the spatial-frequency domain if the conditions

$$T(-k_{x1}, -k_{y1}, k_{x2}, k_{y2}) = \pm T(k_{x1}, k_{y1}, k_{x2}, k_{y2}) \tag{5}$$

hold. Clearly, a specular (antispecular) CSD leads to a specular (antispecular) ACF. Propagation of beam-like fields into a plane $z > z_0$ is governed by the paraxial form of the angular spectrum representation,

$$\begin{aligned} W(x_1, y_1, x_2, y_2, z) = &\iiiint_{-\infty}^{\infty} T(k_{x1}, k_{y1}, k_{x2}, k_{y2}) \exp\left[\frac{i\Delta z}{2k_0}\left(k_{x1}^2 + k_{y1}^2 - k_{x2}^2 - k_{y2}^2\right)\right] \\ &\times \exp\left[-i\left(k_{x1}x_1 + k_{y1}y_1 - k_{x2}x_2 - k_{y2}y_2\right)\right] \mathrm{d}k_{x1} \mathrm{d}k_{y1} \mathrm{d}k_{x2} \mathrm{d}k_{y2}, \end{aligned} \tag{6}$$

where $\Delta z = z - z_0$ and $k_0 = \omega/c = 2\pi/\lambda_0$ is the vacuum wave number at wavelength λ_0. It is readily seen from Eqs. (6) and (4) that the specularity of the CSD is preserved in paraxial propagation, i.e., Eq. (3) holds also for any $z > z_0$.

In practice, the transformation in Eq. (2) can be realized by placing a perfectly aligned WFI, with a phase delay ϕ between the arms, in the Fourier plane of an imaging system as illustrated in

Optics EXPRESS

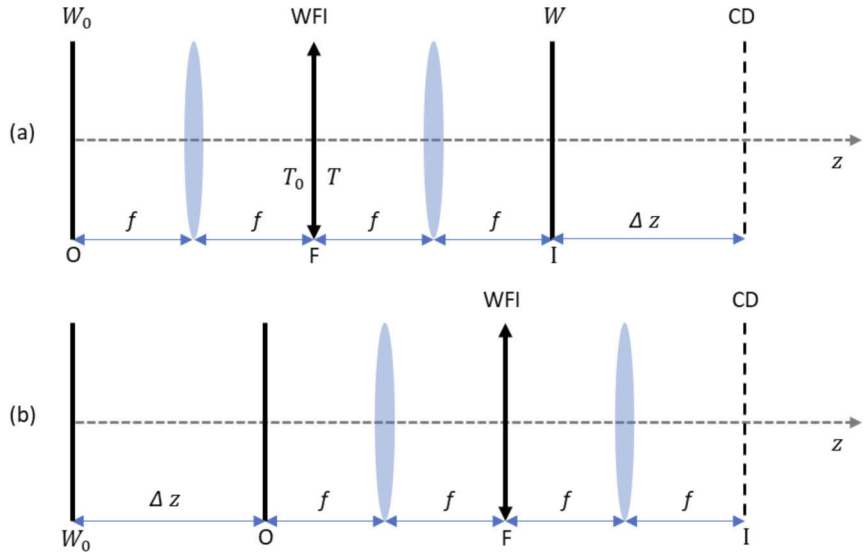

Fig. 1. (a) A linearized schematic of an imaging system for forming specular fields from an arbitrary field in the object plane (O) and a WFI with its folding plane at the Fourier plane (F) of the system. (b) Simplified setup for measuring the propagation properties of specular fields at the image plane (I) of the $4f$ imaging system with a coherence detector CD.

Fig. 1(a). In a traditional WFI implementation with two perpendicularly oriented right-angle prisms, the Fourier plane coincides with the planes of the prism corners. The propagation properties of the field at any distance Δz after the image plane of the system would then be analyzed with a coherence detector (CD), such as another WFI.

In the setup of Fig. 1(a), the WFI acts on the ACF of the field instead of the CSD directly. It transforms the ACF, $T_0(k_{x1}, k_{y1}, k_{x2}, k_{y2})$, of the input spatial field $W_0(x_1, y_2, x_2, y_2, z_0)$ into $T(k_{x1}, k_{y1}, k_{x2}, k_{y2})$ that satisfies Eq. (5). However, since this ACF can be expressed as a superposition analogous to Eq. (2), it is clear by inversion of Eq. (4) that the field after the WFI appears as if it were generated by a virtual source of the form of Eq. (2). This leads to a somewhat simplified system for full characterization of specular fields, as illustrated in Fig. 1(b). Here, the entire imaging system with the WFI in its Fourier plane and the coherence detector at its image plane, is moved along the z-axis. A system of this type will be employed in our experiments, except that we will use a single-lens imaging setup. As a final note at this point, the location of the WFI at the Fourier plane is not critical. Being a non-imaging device, we can place the WFI quite freely within the Fourier space of the system.

3. New class of Bessel-correlated specular beams

The specular transformation given by Eq. (2) has thus far been applied to a few specific CSDs. If applied to a fundamental Bessel-correlated Schell model plane wave, it leads to a propagation-invariant field with either a bright central peak (specular case) or a dark dip (antispecular case) on a uniform background [4,7,8]. Applying it to a conventional Gaussian Schell-model (GSM) beam leads to a specular (antispecular) field with a non-Gaussian intensity profile having a central peak (dip) whose width depends on the degree of coherence of the original GSM beam [4].

Here we consider a recently introduced class of Bessel-correlated fields [9,10], which do not generally obey the Schell model. The free-space propagation properties of these fields are known, and under certain conditions they can be self-Fourier-transforming in the sense that $W_0(x_1, y_2, x_2, y_2, z_0)$ and $T_0(k_{x1}, k_{y1}, k_{x2}, k_{y2})$ have exactly the same functional form. Experimental

Optics EXPRESS

generation of such fields is possible with rotating deterministic devices as illustrated in Fig. 2 [9,10]. We proceed with a summary of the theory for a wedge in Fig. 2(a), but the case of a plane-parallel plate in Fig. 2(b), which we consider in the experimental demonstrations, follows as a special case. We note that more general rotating devises could also be used, which might for instance include diffractive structures on either surface of the wedge or the plate.

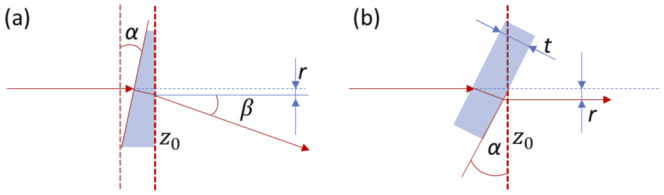

Fig. 2. Generation of the incident CSD by rotating devices such as (a) a wedge of central thickness t and wedge angle α or (b) a glass plate of thickness t inclined by an angle α. The axis of the output beam draws of cone (wedge) or a cylinder (plane-parallel plate) when the device is rotated.

We assume illumination by a Gaussian beam, whose axis coincides with the rotation axis of the device and has its waist at the output plane $z = z_0$ of the device, indicated by the dashed vertical line. The optical axis of the output beam then draws a cone characterized by radius r and cone angle β in the case of the wedge, these parameters being directly related to the prism parameters t and α. In the case of the plane-parallel plate $\beta = 0$ and the the output-beam axis draws a cylinder of radius r. In both cases, the entire partially coherent beam can be interpreted as an incoherent superposition of fully coherent 'elementary' Gaussian beams in time-averaged sense [9,10]. The time average due to rotation can also be understood as an ensemble average over space-frequency domain field realizations corresponding to different rotation angles, with all realizations having an equal probability of occurrence.

The propagation properties of fields generated by rotating wedges have been derived in Ref. [10]. In summary, the CSD at any distance Δz from the source plane $z = z_0$ is given by the formula

$$W(x_1, y_1, x_2, y_2, z) = S_0 \frac{w_0^2}{w^2(z)} \exp\left[-\frac{x_1^2 + x_2^2 + y_1^2 + y_2^2 + 2\,(r - \Delta z \sin\beta)^2}{w^2(z)}\right] \times I_0\left[a(x_1, y_1, x_2, y_2, z)\right] \exp\left[\frac{ik_0}{2R(z)}\left(x_2^2 - x_1^2 + y_2^2 - y_1^2\right)\right], \tag{7}$$

where I_0 is a modified Bessel function of the first kind and order zero and

$$a(x_1, y_1, x_2, y_2, z) = \frac{4r}{w^2(z)} \left\{\left[\left(1 + \frac{\Delta z}{r}\sin\beta\right)\bar{x} - i\left(\frac{\Delta z}{z_\mathrm{R}} + \frac{z_\mathrm{R}}{r}\sin\beta\right)\frac{\Delta x}{2}\right]^2 + \left[\left(1 + \frac{\Delta z}{r}\sin\beta\right)\bar{y} - i\left(\frac{\Delta z}{z_\mathrm{R}} + \frac{z_\mathrm{R}}{r}\sin\beta\right)\frac{\Delta y}{2}\right]^2\right\}^{1/2}, \tag{8}$$

where we have introduced the average and difference coordinates $\bar{x} = (x_1 + x_2)/2$, $\bar{y} = (y_1 + y_2)/2$, $\Delta x = x_2 - x_1$, $\Delta y = y_2 - y_1$. Furthermore, we have employed the usual Gaussian-beam propagation parameters, i.e., the radius of the wave-front curvature

$$R(z) = \Delta z + z_\mathrm{R}^2/\Delta z \tag{9}$$

and the beam width

$$w(z) = w_0\left[1 + (\Delta z/z_\mathrm{R})^2\right]^{1/2}, \tag{10}$$

where $z_\mathrm{R} = k_0 w_0^2/2$ is the Rayleigh range of the incident Gaussian beam.

Optics EXPRESS

The CSD of the beam after the specular transformation is obtained by inserting from Eq. (7) into Eq. (2). By defining

$$b(x_1,y_1,x_2,y_2,z)=\frac{4r}{w^2(z)}\left\{\left[\left(\frac{\Delta z}{z_{\mathrm{R}}}+\frac{z_{\mathrm{R}}}{r}\sin\beta\right)\bar{x}+i\left(1+\frac{\Delta z}{r}\sin\beta\right)\frac{\Delta x}{2}\right]^2 + \left[\left(\frac{\Delta z}{z_{\mathrm{R}}}+\frac{z_{\mathrm{R}}}{r}\sin\beta\right)\bar{y}+i\left(1+\frac{\Delta z}{r}\sin\beta\right)\frac{\Delta y}{2}\right]^2\right\}^{1/2} \tag{11}$$

we obtain

$$W(x_1,y_1,x_2,y_2,z)=S_0\frac{w_0^2}{w^2(z)}\exp\left[-\frac{x_1^2+x_2^2+y_1^2+y_2^2+2\,(r-\Delta z\sin\beta)^2}{w^2(z)}\right] \times\{I_0[a(x_1,y_1,x_2,y_2,z)]+J_0[b(x_1,y_1,x_2,y_2,z)]\cos\phi\} \times\exp\left[\frac{ik_0}{2R(z)}\left(x_2^2-x_1^2+y_2^2-y_1^2\right)\right], \tag{12}$$

where J_0 is a Bessel function of the first kind and order zero.

We can also write Eq. (12) entirely in terms of the average and difference coordinates and extract the spherical phase term by writing the CSD in the form

$$W(\bar{x},\bar{y},\Delta x,\Delta y,z)=W_{\mathrm{r}}(\bar{x},\bar{y},\Delta x,\Delta y,z)\exp\left[\frac{ik_0}{R(z)}\left(\bar{x}\Delta x+\bar{y}\Delta y\right)\right], \tag{13}$$

where

$$W_{\mathrm{r}}(\bar{x},\bar{y},\Delta x,\Delta y,z)=S_0\frac{w_0^2}{w^2(z)}\exp\left[-\frac{2\,(r-\Delta z\sin\beta)^2}{w^2(z)}\right]\exp\left[-\frac{2\left(\bar{x}^2+\bar{y}^2\right)}{w^2(z)}\right]\exp\left[-\frac{\Delta x^2+\Delta y^2}{2w^2(z)}\right] \times\{I_0[a(\bar{x},\bar{y},\Delta x,\Delta y,z)]+J_0[b(\bar{x},\bar{y},\Delta x,\Delta y,z)]\cos\phi\} \tag{14}$$

is the 'reduced' CSD. This reduced form has the advantage that its phase (and that of the reduced complex degree of coherence) only contains the difference from the propagation-induced spherical phase. A corresponding expression for the incident field is obtained by dropping the J_0 contribution (setting $\phi=\pi/2$). Finally, the evolution of the CSD in the far zone $\Delta z\gg z_{\mathrm{R}}$ of the Gaussian elementary beam follows from Eqs. (13) and (14) in the asymptotic limits $R(z)\to\Delta z$ and $w(z)\to w_0\Delta z/z_{\mathrm{R}}$.

4. Physical properties of Bessel-correlated specular fields

We proceed to illustrate the main physical features of the specular fields under consideration. Our interest is, in particular, to clarify the effects of the specular transformation on the beam properties. We could analyze these for any combination of the parameters r and β, but choose to restrict the attention to the special case $\beta=0$ to reduce the number of degrees of freedom and thereby keep the number of figures at a reasonable level. As already mentioned, this choice corresponds to the plane-parallel plate geometry of Fig. 1(b).

It is convenient at this stage to introduce dimensionless (z-dependent) transverse coordinates $\tilde{x}=\bar{x}/w(z)$, $\tilde{y}=\bar{y}/w(z)$, $\Delta\tilde{x}=\Delta x/w(z)$, $\Delta\tilde{y}=\Delta y/w(z)$, a normalized parameter $\tilde{r}=r/w_0$, and a

Optics EXPRESS

propagation parameter

$$D(z) = \left[1 + (\Delta z/z_{\mathrm{R}})^2\right]^{1/2}. \tag{15}$$

Then, in the special case $\beta = 0$, Eq. (14) takes the form

$$W_{\mathrm{r}}(\tilde{x}, \tilde{y}, \Delta\tilde{x}, \Delta\tilde{y}, z) = C(z) \exp\left[-2\left(\tilde{x}^2 + \tilde{y}^2\right)\right] \exp\left[-\frac{1}{2}\left(\Delta\tilde{x}^2 + \Delta\tilde{y}^2\right)\right] \times \{I_0[a(\tilde{x}, \tilde{y}, \Delta\tilde{x}, \Delta\tilde{y}, z)] + J_0[b(\tilde{x}, \tilde{y}, \Delta\tilde{x}, \Delta\tilde{y}, z)] \cos\phi\}, \tag{16}$$

where

$$C(z) = \frac{S_0}{D^2(z)} \exp\left(-\frac{2\tilde{r}^2}{D^2(z)}\right), \tag{17}$$

is a z-dependent scaling factor and

$$a(\tilde{x}, \tilde{y}, \Delta\tilde{x}, \Delta\tilde{y}, z) = \frac{4\tilde{r}}{D(z)} \left[\left(\tilde{x} - i\frac{\Delta z}{z_{\mathrm{R}}}\frac{\Delta\tilde{x}}{2}\right)^2 + \left(\tilde{y} - i\frac{\Delta z}{z_{\mathrm{R}}}\frac{\Delta\tilde{y}}{2}\right)^2\right]^{1/2}, \tag{18}$$

$$b(\tilde{x}, \tilde{y}, \Delta\tilde{x}, \Delta\tilde{y}, z) = \frac{4\tilde{r}}{D(z)} \left[\left(\frac{\Delta z}{z_{\mathrm{R}}}\tilde{x} + i\frac{\Delta\tilde{x}}{2}\right)^2 + \left(\frac{\Delta z}{z_{\mathrm{R}}}\tilde{y} + i\frac{\Delta\tilde{y}}{2}\right)^2\right]^{1/2}. \tag{19}$$

The spectral density of the field is given by

$$S(\tilde{x}, \tilde{y}, z) = C(z) \exp\left[-2\left(\tilde{x}^2 + \tilde{y}^2\right)\right] \left\{I_0[a(\tilde{x}, \tilde{y}, z)] + J_0\left[\frac{\Delta z}{z_{\mathrm{R}}} a(\tilde{x}, \tilde{y}, z)\right] \cos\phi\right\} \tag{20}$$

with

$$a(\tilde{x}, \tilde{y}, z) = \frac{4\tilde{r}}{D(z)} \left(\tilde{x}^2 + \tilde{y}^2\right)^{1/2}, \tag{21}$$

and the complex degree of spatial coherence (DOC) can be found by normalizing the CSD with the spectral density as in

$$\mu_{\mathrm{r}}(\tilde{x}, \tilde{y}, \Delta\tilde{x}, \Delta\tilde{y}, z) = \frac{W_{\mathrm{r}}(\tilde{x}, \tilde{y}, \Delta\tilde{x}, \Delta\tilde{y}, z)}{\sqrt{S(\tilde{x} + \Delta\tilde{x}/2, \tilde{y} + \Delta\tilde{y}/2, z) S(\tilde{x} + \Delta\tilde{x}/2, \tilde{y} + \Delta\tilde{y}/2, z)}}. \tag{22}$$

This reduced DOC is real-valued and attains values between -1 and $+1$, corresponding to perfect anticorrelation and correlation, respectively.

It is of particular interest to consider the propagation of the field into the far zone. In the special case $\beta = 0$ we can interpret the full partially coherent beam as an incoherent superposition of elementary Gaussian beams originating from a ring of radius r and propagating in parallel. In the far zone of each elementary beam, we have $D(z) \to \Delta z/z_{\mathrm{R}}$ and $w(z) \to w_0 \Delta z/z_{\mathrm{R}}$. In this limit the spectral density distribution takes on the form

$$S(\tilde{x}, \tilde{y}, z) = C(z) \exp\left[-2\left(\tilde{x}^2 + \tilde{y}^2\right)\right] \left\{I_0\left[\frac{4\tilde{r} z_{\mathrm{R}}}{\Delta z}\left(\tilde{x}^2 + \tilde{y}^2\right)^{1/2}\right] + J_0\left[4\tilde{r}\left(\tilde{x}^2 + \tilde{y}^2\right)^{1/2}\right] \cos\phi\right\}, \tag{23}$$

where $C(z) = S_0 (z_{\mathrm{R}}/\Delta z)^2 \exp\left[-2\tilde{r}(z_{\mathrm{R}}/\Delta z)^2\right]$. The far-zone region for the entire partially coherent beam is achieved when $\Delta z \gg 4\tilde{r} z_{\mathrm{R}}$, in which case we have the limit

$$S(\tilde{x}, \tilde{y}, z) = C(z) \exp\left[-2\left(\tilde{x}^2 + \tilde{y}^2\right)\right] \left\{1 + J_0\left[4\tilde{r}\left(\tilde{x}^2 + \tilde{y}^2\right)^{1/2}\right] \cos\phi\right\}. \tag{24}$$

By introducing a paraxial-domain diffraction angle $\theta = \sqrt{x^2 + y^2}/\Delta z$ we can write this result in the form

$$S(\theta, z) = C(z) \exp\left[-2(\theta/\theta_0)^2\right] \left[1 + J_0(4\tilde{r}\theta/\theta_0) \cos\phi\right], \tag{25}$$

where $\theta_0 = \lambda_0/\pi w_0$ is the divergence angle of the incident Gaussian beam (and of each elementary Gaussian beam in the elementary-field superposition of the field prior to the specular

Optics EXPRESS

transformation). It is evident from this expression that the specular far-zone field exhibits spatial intensity oscillations on a scale sharper than the classical diffraction limit of the incident field (given by the Gaussian distribution with divergence angle θ_0) would suggest. These oscillations are reminiscent to those in, e.g., spatially coherent Bessel–Gauss beams [11], which can be expressed as coherent superpositions of Gaussian beams. In our case we have an incoherent superposition (if $\tilde{r}>0$); evidently, the intensity oscillations are due to the specularity of the resulting partially coherent field since they vanish in the non-specular case $\phi = \pi/2$ (and also if $\tilde{r} = 0$).

5. Numerical illustrations

We proceed to illustrate the effects of the specular transformation in three representative cases: at the source plane $\Delta z = 0$, at a propagation distance $\Delta z = z_{\mathrm{R}}$ equal to one Rayleigh range of the incident beam, and in the far field region $\Delta z \gg 4\tilde{r} z_{\mathrm{R}}$. Figure 3 illustrates the intensity profiles of the fields for some selected ratios $\tilde{r}$. The left and right columns show the profiles for specular ($\phi = 0$) and antispecular ($\phi = \pi$) beams, whereas the middle column displays the profiles in the non-specular ($\phi = \pi/2$) case, which corresponds to the beam before the specular transformation.

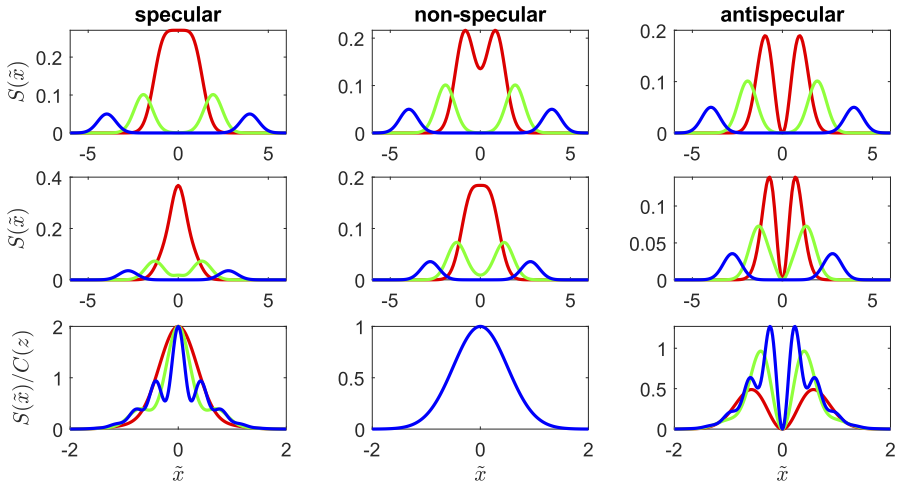

Fig. 3. Cross sections $S(\tilde{x}, 0, z)$ of intensity profiles for specular, non-specular, and antispecular beams at three different propagation distances. Upper row: $z = 0$. Middle row: $z = z_{\mathrm{R}}$. Bottom row: $z \gg z_{\mathrm{R}}$. Red: $\tilde{r} = 1$. Green: $\tilde{r} = 2$. Blue: $\tilde{r} = 4$.

Considering first the non-specular (incident) case, the 'elementary' Gaussian beams that make up the Bessel-correlated beam as the plate rotates are centered on a ring of radius $\tilde{r}$ at the source plane $\Delta z = 0$. The doughnut shape of the intensity profile is apparent already at $\tilde{r} = 1$ and becomes increasingly clear for larger values. The propagation axes of the elementary beams lie on a cylinder of radius $\tilde{r}$, and diffractive spreading causes the beams to overlap once they have propagated far enough, leading to gradual weakening of the doughnut shape. In the far field, all elementary beams overlap completely, resulting in a Gaussian profile regardless of $\tilde{r}$.

In the specular and antispecular cases the I_0 and J_0 contributions add up, with either a positive or a negative sign for the latter. In the antispecular case this leads to zero intensity on the optical axis at all propagation distances and values of $\tilde{r}$. In the specular case the axial intensity is always non-zero: at the source plane we observe a nearly flat-top intensity profile if $\tilde{r} = 1$. The doughnut shape is preserved at the source plane when $\tilde{r}$ is increased, whether the field is specular or antispecular. Diffraction ultimately smooths out the doughnut shape, and in the far field the side lobes due to the J_0 contribution become apparent when $\tilde{r}$ increases. These side lobes lead to

Optics EXPRESS

'superoscillating' far-field intensity profiles, featuring sharper variations than a non-specular field can have. The oscillations result from partial spatial coherence of the field; their role becomes increasingly evident when the degree of coherence of the input beam is reduced by increasing the ratio $\tilde{r}$.

Since the fields considered here are of the Schell-model form only in special cases, the CSD and the associated complex degree of coherence are 4D functions, of which we can conveniently present only 2D slices. We choose cuts of the form $W_{\mathrm{r}}(0, \tilde{y}, \Delta\tilde{x}, 0, z)$, which corresponds to what our coherence characterization device can measure in a single-shot manner (as described below). One can also argue that this choice is the most intuitive one since, according to Eqs. (16)–19, $\mu_{\mathrm{r}}(0, \tilde{y}, \Delta\tilde{x}, 0, z)$ is real-valued. Figure 4 illustrates slices $\mu_{\mathrm{r}}(0, \tilde{y}, \Delta\tilde{x}, 0, z)$ of the reduced degree of coherence for $\tilde{r} = 1$ and $\tilde{r} = 4$.

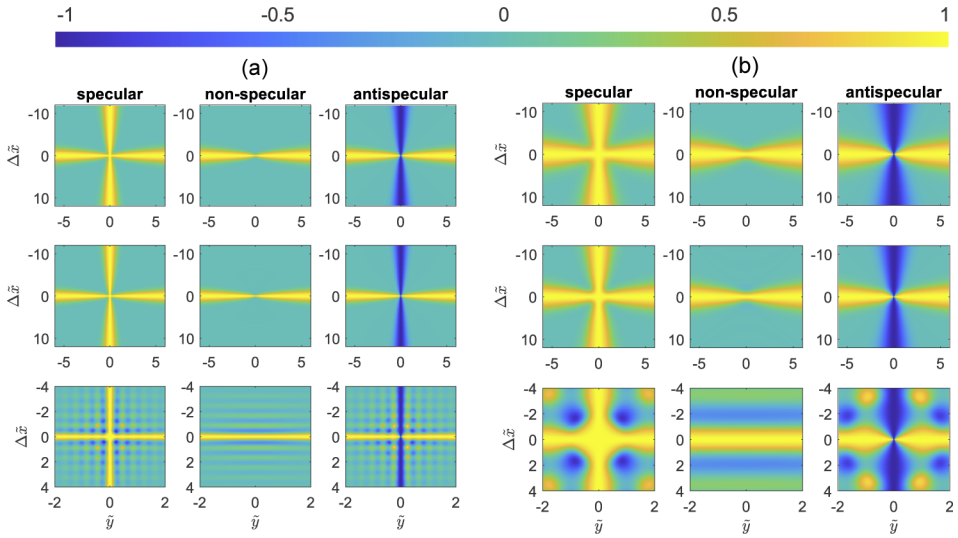

Fig. 4. Reduced degree of coherence $\mu_{\mathrm{r}}(0, \tilde{y}, \Delta\tilde{x}, 0, z)$ in the $(\tilde{y}, \Delta\tilde{x})$ coordinate system when $\tilde{r} = 1$ (left) and $\tilde{r} = 4$ (right). Upper row: $\Delta z = 0$. Middle row: $\Delta z = z_{\mathrm{R}}$. Lower row: $\Delta z \gg 4\tilde{r} z_{\mathrm{R}}$.

In general, increasing $\tilde{r}$ leads to a richer texture in distributions of the reduced degree of coherence. At the source plane the distribution of $\mu_{\mathrm{r}}(0, \tilde{y}, \Delta\tilde{x}, 0, 0)$ associated with the incident beam is non-negative, but propagation introduces also negative values (phase changes by π radians). In the far zone we have a Schell-model Bessel-correlated ($\tilde{y}$-invariant) field with prominent side lobes. The characteristic cross-like symmetry (asymmetry) of specular (antispecular) fields becomes apparent in the plots of $\mu_{\mathrm{r}}(0, \tilde{y}, \Delta\tilde{x}, 0, z)$. In particular, we have $\mu_{\mathrm{r}}(0, \tilde{y}, 0, 0, 0, z) = \mu_{\mathrm{r}}(0, 0, \Delta\tilde{x}, 0, z) = 1$ for specular fields and $\mu_{\mathrm{r}}(0, \tilde{y}, 0, 0, z) = 1$ while $\mu_{\mathrm{r}}(0, 0, \Delta\tilde{x}, 0, z) = -1$ for antispecular fields at all propagation distances.

6. Experimental results

The principle of our experimental setup is as illustrated in Fig. 1(b). A rotating plate, illuminated by a Gaussian beam of width w_0, is used to generate a Bessel beam characterized by a radius parameter r as in Fig. 2(b). The specular (antispecular) transformation is implemented by a 2D mirror-based WFI illustrated in Fig. 5(a) and the coherence detector CD by a traditional 1D folding WFI shown in Fig. 5(b).

Optics EXPRESS

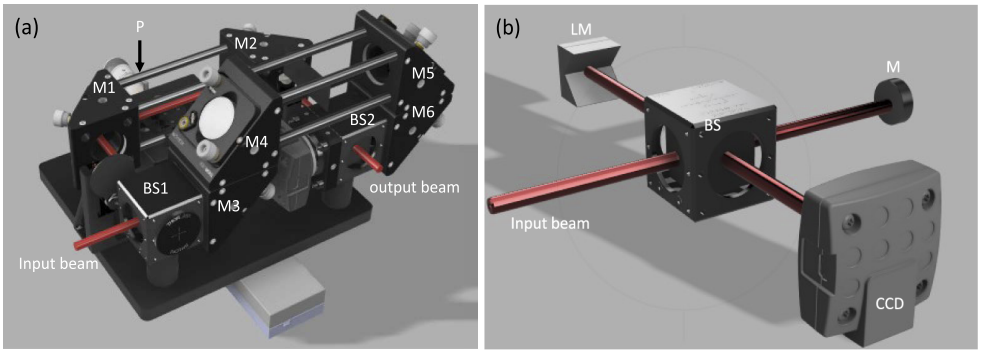

Fig. 5. (a) The 2D WFI for the specular transformation. Here M1–M6 are planar mirrors, BS1 and BS2 are beam splitters, and P is piezo-electric stage. (b) The 1D WFI for beam characterization. Here BS is a beam splitter, M is a planar mirror, LM is a retroreflecting mirror, and CCD is a camera.

Instead of the $4f$ imaging system assumed in Fig. 1(b), we used a single-lens imaging system with a magnification of M. Hence, the field at the plane I in Fig. 1(b) is characterized by a CSD

$$W(\bar{x},\bar{y},\Delta x,\Delta y,z_{\rm I}) = \frac{1}{M^2} W\left(\frac{\bar{x}}{M},\frac{\bar{y}}{M},\frac{\Delta x}{M},\frac{\Delta y}{M},z\right) \exp\left[-\frac{ik_0}{Mf}\left(\bar{x}\Delta x+\bar{y}\Delta y\right)\right]. \tag{26}$$

Inserting from Eq. (13) gives

$$W(\bar{x},\bar{y},\Delta x,\Delta y,z_{\rm I}) = \frac{1}{M^2} W_{\rm r}\left(\frac{\bar{x}}{M},\frac{\bar{y}}{M},\frac{\Delta x}{M},\frac{\Delta y}{M},z\right) \exp\left[\frac{ik_0}{R(z_{\rm I})}\left(\bar{x}\Delta x+\bar{y}\Delta y\right)\right], \tag{27}$$

where the image-plane radius of wavefront curvature $R(z_{\rm I})$ is given by

$$\frac{1}{R(z_{\rm I})} = \frac{1}{R(z)} - \frac{1}{Mf}. \tag{28}$$

The 1D WFI in Fig. 5(b) measures slices $W(\bar{x},\bar{y},\Delta x,0,z_{\rm I})$ if its folding axis is scanned along $\bar{x}$. When $\bar{x}=0$, it therefore produces direct access to (magnified) cross sections $W_{\rm r}(0,\bar{y},\Delta x,0,z)$ of the reduced CSD, since the spherical phase term in Eq. (27) vanishes.

In our experimental implementation of the setup, we used a lens with 50 mm focal length to focus a HeNe beam with $\lambda_0 = 632.8$ nm on a 3 mm thick rotating glass plate to produce a Bessel-correlated beam with parameters $w_0 \approx 22.3$ μm and $r \approx 29.1$ μm, which give $z_{\rm R} \approx 2.47$ mm and $\tilde{r} \approx 1.3$. An imaging lens of focal length 150 mm was used to produce an image of the O plane with magnification $M \approx -10$ onto the I plane. The phase ϕ was tuned with a piezo-electric stage in one arm to produce specular ($\phi = 0$), non-specular ($\phi = \pi/2$, corresponding to the incident beam), and antispecular ($\phi = \pi$) beams. Figure 6 shows snapshots of the cross sections $\bar{y} = 0$ of the intensity patterns produced directly by the 1D WFI in the specular, non-specular, and antispecular cases. The associated video shows the directly measured 2D interference patterns when the piezo is tuned to vary the phase ϕ over an interval of π radians.

Figure 7 shows simulated and measured intensity distributions of specular, non-specular, and antispecular fields at three selected propagation distances $\Delta z = 0$, $\Delta z = 4$ mm $\approx 1.6 z_{\rm R}$, and $\Delta z = 13$ mm $\approx 5.3 z_{\rm R}$ (the slight interference patterns seen in the experimental results arise from the coating on top of CCD). The non-specular case was measured by setting $\phi = \pi/2$ in the 2D WFI, instead of measuring the incident beam directly.

In the non-specular case, the doughnut shape has disappeared at $\Delta z = 4$ mm and the beam has expanded at $\Delta z = 13$ mm, where the far field condition is yet fully satisfied. In the specular

Optics EXPRESS

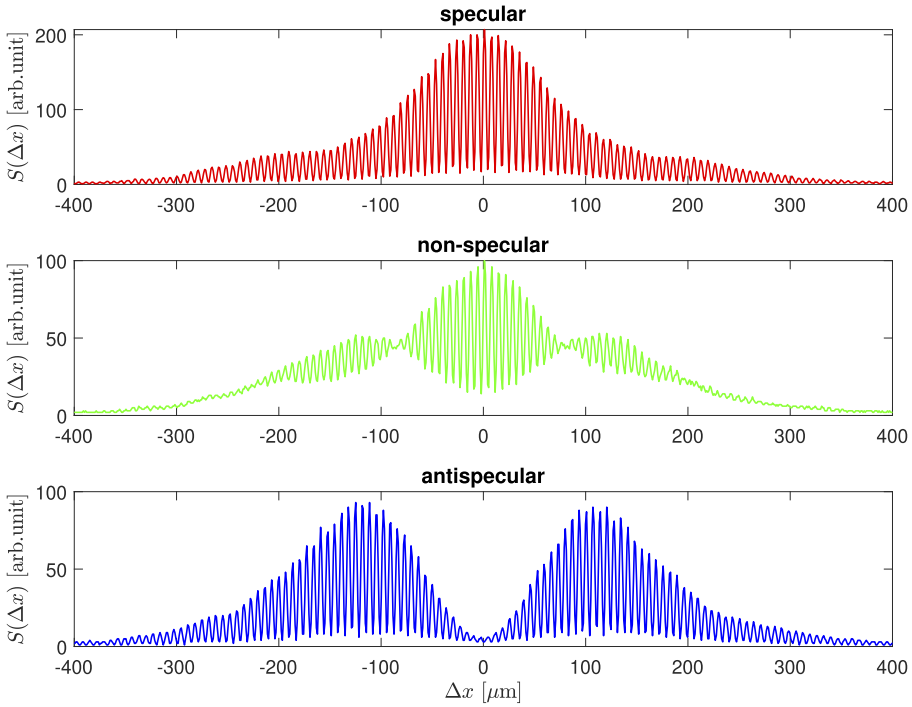

Fig. 6. Interference patterns observed directly by the 1D WFI at $\bar{y} = 0$ and $\Delta z = 13$ mm in specular (top row), non-specular (middle row), and antispecular (bottom row) cases. The transition of the measured interference pattern from specular to antispecular case is captured and presented in the Visualization 1

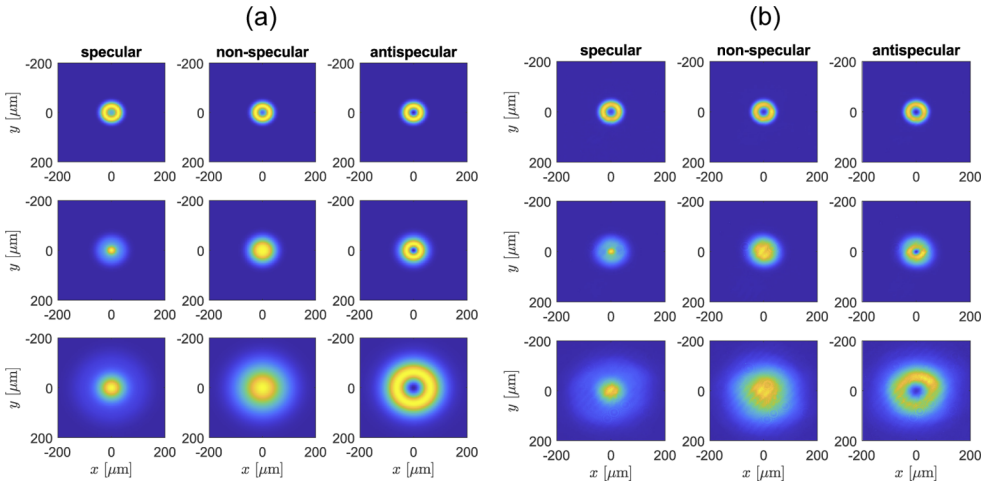

Fig. 7. Simulated (a) and measured (b) intensity distributions of specular (left columns), non-specular (middle columms), and antispecular (right columns) Bessel-correlated fields at propagation distance $\Delta z = 0$ (top rows), $\Delta z = 4$ mm (middle rows), and $\Delta z = 13$ mm (bottom rows).

case characteristic central peaks and some side-lobe structure emerge at $\Delta z = 4$ mm, and become clearer when the far field is approached at $\Delta z = 13$ mm, where the 'superoscillating' nature of

Optics EXPRESS

the intensity profile is already visible. Finally, in the antispecular case, the central dip that is preserved at all propagation distances, is clearly observed also experimentally. The simulated and measured distributions of $W(0, \bar{y}, \Delta x, 0)$ are plotted in Fig. 8 at the three propagation distances $\Delta z = 0$, $\Delta z = 4$ mm, and $\Delta z = 13$ mm for the specular, non-specular, and antispecular cases. The retrieval process of the experimental CSD is outlined in the Appendix.

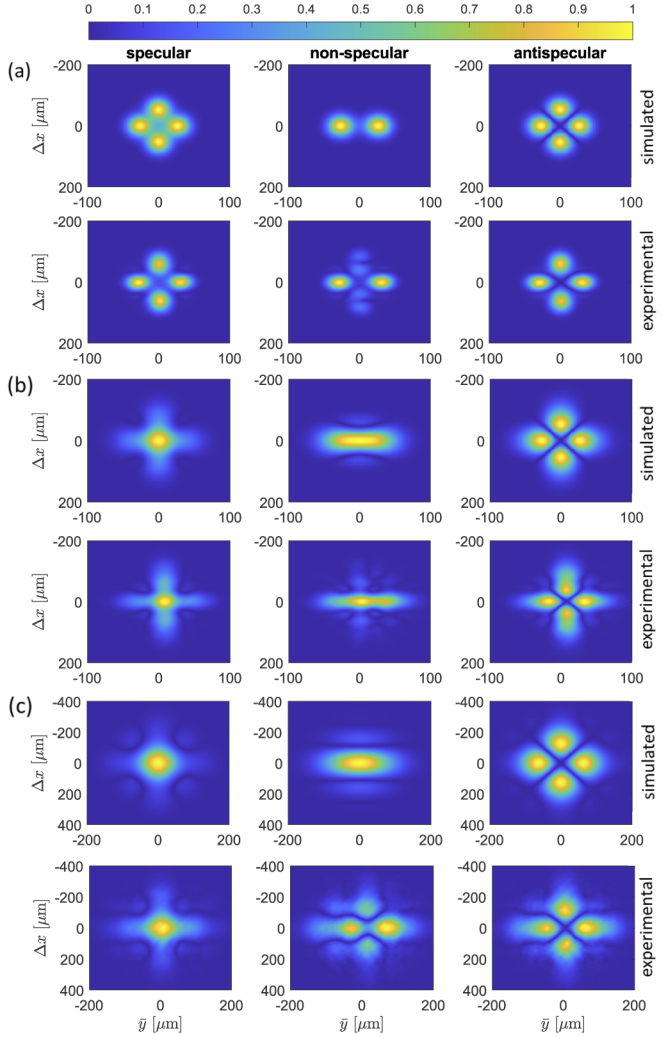

Fig. 8. Normalized CSD in the $(\bar{y}, \Delta x)$ coordinate system. (a) $\Delta z = 0$. (b) $\Delta z = 4$ mm. (c) $\Delta z = 13$ mm. In each case the upper rows represent simulated results and the lower rows are experimental. Left columns: $\phi = 0$. Middle columns: $\phi = \pi/2$. Right columns: $\phi = \pi$. The transformation from specular to anti-specular CSD (both simulated and measured) in the case of $\Delta z = 0$ mm and $\Delta z = 4$ mm are presented in Visualization 2, Visualization 3.

Clearly, the simulations and the experiments match fairly well, especially for the specular case. At larger propagation distances the deviations become somewhat more pronounced. Remarkably, this is the case in particular for the non-specular beam, whereas the characteristic cross shapes of the specular and non-specular beams (which are of main interest here) are much better preserved on propagation. We stress, however, once again that the non-specular beam was generated by setting $\phi = \pi/2$ in the 2D WFI instead of measuring the (non-specular) incident beam directly.

Optics EXPRESS

7. Conclusions and remarks

We have presented a scheme for carrying out the specular transformation implied in Eq. (2), and to study the propagation of the resulting beams. Specifically, a mirror-based WFI with a controllable phase difference between the optical paths along the two arms was used to produce the specular transform of Bessel-correlated input fields, and a 1D-folding WFI was used to characterize the properties of the generated beams. In particular, we demonstrated that specular beams have 'super-oscillating' far-zone intensity profiles due to the partial degree of spatial coherence of the input beam. Such oscillations would appear also in the focal regions of optical systems. These oscillations may appear somewhat analogous to super-oscillations of coherent fields, which imply superresolution beyond the diffraction limit in microscopy [12,13]. To avoid potential misinterpretations, we stress that in our case the oscillations become more rapid when the source coherence is decreased by increasing $\tilde{r}$. However, this comes only at the cost of simultaneously increasing the effective source size. Hence, considering a focusing system with given numerical aperture NA, decreasing spatial coherence ultimately results in truncation of the source field by the NA.

Although we have applied the method to a particular class of Bessel-correlated input beams, it could equally well be applied to any partially spatially coherent scalar beam. An obvious next step would be to apply the specular transform to electromagnetic beams with arbitrary partial coherence and polarization properties; in fact some work in this direction has already been reported [14]. When applied to coherence measurement, the mirror-based WFI produces only negligible polarization-dependent effects [5,6]. However, our preliminary analysis shows that a WFI can produce a number of interesting polarization-dependent effects when used as a device for transforming electromagnetic beams into specular (or antispecular) form. For instance, the WFI may alter the polarization state and the degree of polarization of a fully polarized (circular or elliptical) spatially partially coherent input beam. In the case of an electromagnetic specular (or antispecular) beam, one may not observe an intensity peak (or dip), but rather a polarization peak or dip. Altogether, there exists plenty of scope for further investigation on the specular transform of electromagnetic beams with arbitrary partial coherence and polarization properties.

Appendix

Fig. 9 illustrates the process of extracting the coherence properties of the field. In order to construct the CSD function, at least three frames are generally needed [5,6]. However, since the beam profile is rotationally symmetric and we measure CSD in coordinates $(\bar{y}, \Delta x)$ using a 1D WFI, a single measurement of the interference is sufficient. Figure 9(a) shows an example of such measured interference fringes when a linear wavefront tilt has been introduced in the x direction.

This interference pattern can be represented as a superposition of three terms. The first is a DC term determined by the (rotationally symmetric) intensity profile of the incident field, centered at the zero spatial frequency in the Fourier space. The second and third terms are proportional to the (real-valued) function $W_{\mathrm{r}}(0, \bar{y}, \Delta x, 0)$, and their Fourier transforms are centered at off-axis points in the spatial-frequency space. Hence, Fourier transforming the measured fringe profile (numerically) leads to results like illustrated in Fig. 9(b), where the DC terms is placed inside the solid box. We can now extract one of the off-axis terms, such as the one inside the dashed box in Fig. 9(b). Then the distribution of $W_{\mathrm{r}}(0, \bar{y}, \Delta x, 0)$ can be retrieved by calculating the inverse Fourier transform. The result is shown in Fig. 9(c). Consequently, the intensity distribution and the complex degree of spatial coherence can be calculated, resulting in Figs. 9(d)–(f).

In Fig. 9 we have illustrated the antispecular beam at $z = 0$ mm as an example. Hence, ideally, the phase of the complex degree of spatial coherence should be binary (either zero or π). As expected, the retrieved phase profile is of binary form only approximately.

Optics EXPRESS

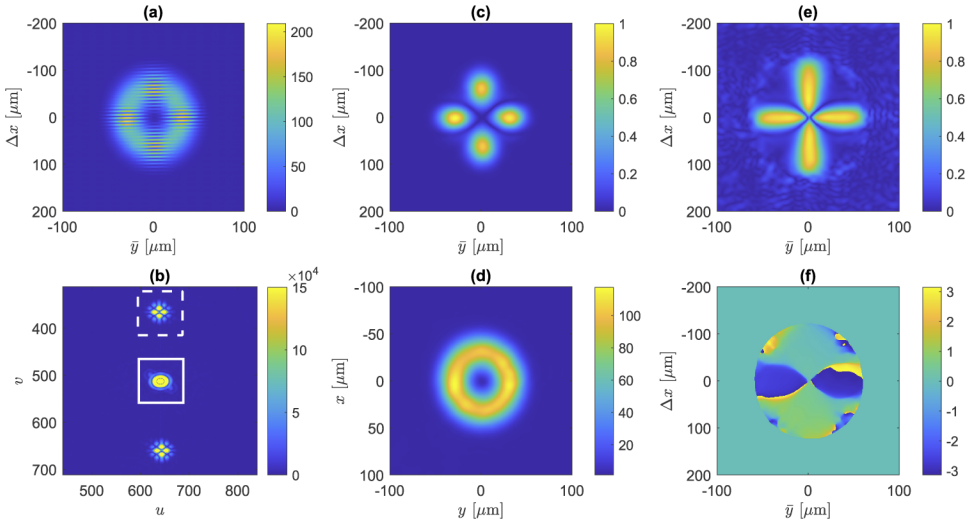

Fig. 9. Extraction of the intensity and complex degree of coherence from measured fringe patterns. As an example we have chosen the antispecular beam at $z = 0$ mm. (a) Directly measure fringe pattern. (b) Numerically calculated Fourier transform of the intensity pattern. (c) Inverse Fourier of the extracted part, giving $W_r(0, \bar{y}, \Delta x, 0)$. (d) The retrieved spatial intensity profile $S(x, y)$. (e) The retrieved absolute value of the complex degree of coherence $\mu_r(0, \bar{y}, \Delta x, 0)$. (f) The retrieved phase of $\mu_r(0, \bar{y}, \Delta x, 0)$.

Funding. Academy of Finland (320165, 320166, 333938).

Disclosures. The authors declare no conflicts of interests.

Data availability. Data underlying the results presented in this paper are not publicly available at this time but may be obtained from the authors upon reasonable request.

References

1. P. De Santis, F. Gori, G. Guattari, and C. Palma, "A space-time modulated field with specular coherence function," Opt. Commun. **64**(1), 9–14 (1987).
2. F. Gori, G. Guattari, C. Palma, and C. Padovani, "Specular cross-spectral density functions," Opt. Commun. **68**(4), 239–243 (1988).
3. P. De Santis, F. Gori, M. Santarsiero, and G. Guattari, "Sources with spatially sinusoidal modes," Opt. Commun. **82**(1-2), 123–129 (1991).
4. H. Partanen, N. Sharmin, J. Tervo, and J. Turunen, "Specular and antispecular light beams," Opt. Express **23**(22), 28718–28727 (2015).
5. M. Koivurova, H. Partanen, J. Lahyani, N. Cariou, and J. Turunen, "Scanning wavefront-folding interferometers," Opt. Express **27**(5), 7738–7750 (2019).
6. A. Halder, H. Partanen, A. Leinonen, M. Koivurova, T. K. Hakala, T. Setälä, J. Turunen, and A. T. Friberg, "Mirror-based scanning wavefront-folding interferometer for coherence measurements," Opt. Lett. **45**(15), 4260–4263 (2020).
7. J. Turunen, A. Vasara, and A. T. Friberg, "Propagation-invariance and self-imaging in variable-coherence optics," J. Opt. Soc. Am. A **8**(2), 282–289 (1991).
8. S. A. Ponomarenko, W. Huang, and M. Cada, "Dark and antidark diffraction-free beams," Opt. Lett. **32**(17), 2508–2510 (2007).
9. M. Koivurova, A. Halder, H. Partanen, and J. Turunen, "Bessel-correlated supercontinuum fields," Opt. Express **25**(20), 23974 (2017).
10. A. Halder, M. Koivurova, H. Partanen, and J. Turunen, "Paraxial propagation of a class of Bessel–correlated fields," Opt. Express **26**(8), 11055–11067 (2018).
11. F. Gori, G. Guattari, and C. Padovani, "Bessel–Gauss beams," Opt. Commun. **64**(6), 491–495 (1987).
12. F. M. Huang and N. I. Zheludev, "Super-resolution without evanescent waves," Nano Lett. **9**(3), 1249–1254 (2009).
13. H. Hyvärinen, S. Rehman, J. Tervo, J. Turunen, and C. J. R. Sheppard, "Limitations of superoscillation filters in microscopy applications," Opt. Lett. **37**(5), 903–905 (2012).
14. M. Guo and D. Zhao, "Polarization properties of stochastic electromagnetic beams modulated by a wavefront-folding interferometer," Opt. Express **26**(7), 8581–8593 (2018).